Geochemistry, Geophysics, Geosystems®

RESEARCH ARTICLE
10.1029/2022GC010770

Key Points:

- Using equilibrium and decompression experiments, we show that natural embayments partially equilibrate on timescales of magma ascent
- We build upon previous work developing embayments as reliable recorders of magma decompression rates between 0.008–0.05 MPa s^{-1}
- We produce the full range of textures (glassy to vesiculated) observed in natural embayments both inter- and intra-experimentally

Supporting Information:

Supporting Information may be found in the online version of this article.

Correspondence to:

B. Hosseini,
behnazhosseini@montana.edu

Citation:

Hosseini, B., Myers, M. L., Watkins, J. M., & Harris, M. A. (2023). Are we recording? Putting embayment speedometry to the test using high pressure-temperature decompression experiments. *Geochemistry, Geophysics, Geosystems*, *24*, e2022GC010770. https://doi.org/10.1029/2022GC010770

Received 9 NOV 2022
Accepted 17 MAR 2023

Author Contributions:

Conceptualization: Behnaz Hosseini, Madison L. Myers, James M. Watkins
Data curation: Behnaz Hosseini
Formal analysis: Behnaz Hosseini, Madison L. Myers
Funding acquisition: Behnaz Hosseini, Madison L. Myers
Investigation: Behnaz Hosseini, Madison L. Myers, James M. Watkins, Megan A. Harris
Methodology: Behnaz Hosseini, Madison L. Myers, James M. Watkins, Megan A. Harris

Are We Recording? Putting Embayment Speedometry to the Test Using High Pressure-Temperature Decompression Experiments

Behnaz Hosseini[1], **Madison L. Myers**[1], **James M. Watkins**[2], **and Megan A. Harris**[1]

[1]Department of Earth Sciences, Montana State University, Bozeman, MT, USA, [2]Department of Earth Sciences, University of Oregon, Eugene, OR, USA

Abstract Despite its increasing application to estimate magma decompression rates for explosive eruptions, the embayment speedometer has long awaited critical experimental evaluation. We present the first experimental results on the fidelity of natural quartz-hosted embayments in rhyolitic systems as recorders of magma decompression. We conducted two high pressure-temperature isobaric equilibrium experiments and 13 constant-rate, continuous isothermal decompression experiments in a cold-seal pressure vessel where we imposed rates from 0.005 to 0.05 MPa s^{-1} in both H_2O-saturated and mixed-volatile ($H_2O + CO_2$)-saturated systems. In both equilibrium experiments, we successfully re-equilibrated embayment melt to new fluid compositions at 780°C and 150 MPa, confirming the ability of embayments to respond to and record changing environmental conditions. Of the 32 glassy embayments recovered, seven met the criteria previously established for successful geospeedometry and were thus analyzed for their volatile ($H_2O \pm CO_2$) concentrations, with each producing a good model fit and recovering close to the imposed decompression rate. In one H_2O-saturated experiment, modeling H_2O concentration gradients in embayments from three separate crystals resulted in best-fit decompression rates ranging from 0.012 to 0.021 MPa s^{-1}, in close agreement with the imposed rate (0.015 MPa s^{-1}) and attesting to the reproducibility of the technique. For mixed-volatile experiments, we found that a slightly variable starting fluid composition (~2.4–3.5 wt.%) resulted in good fits to both $H_2O + CO_2$ profiles. Overall our experiments provide confidence that the embayment is a robust recorder of constant-rate, continuous decompression, with the model successfully extracting experimental conditions from profiles representing nearly an order of magnitude variation (0.008–0.05 MPa s^{-1}) in decompression rate.

Plain Language Summary Embayments are pockets of melt within crystals that remain in open communication with the surrounding magma, allowing their compositions to change through time. When rising magma carries an embayment-bearing crystal toward the surface, volatiles (e.g., H_2O, CO_2) dissolved in the melt will diffuse through the embayment to maintain equilibrium with the surrounding degassing melt. Upon eruption and rapid cooling, volatile concentration gradients are preserved within embayment channels. This is the basis for the embayment speedometer: the volatile concentration gradients can be directly measured and numerically modeled to estimate the rate of decompression experienced by the magma. Since its formalization over a decade ago, this technique has been applied extensively, with 11 published studies leveraging the embayment speedometer to estimate magma decompression rates for 17 rhyolitic to basaltic explosive eruptions, and several additional studies in preparation. Despite the increasing application of this technique, no work to date has experimentally evaluated embayments to assess their reliability as recorders of magma decompression under controlled conditions. In this study, we use high pressure-temperature decompression experiments to subject embayments to the conditions experienced during magma ascent. We apply numerical models to volatile analyses of the embayments to evaluate how reliably embayments record the imposed conditions.

1. Introduction

Magma decompression in the conduit modulates the kinetic processes (e.g., degassing, crystallization) that influence volcanic eruption style and vigor. The quantification of decompression rate is therefore consequential to understanding the evolution of eruption intensity and the explosive-effusive eruption transition (e.g., Cassidy et al., 2018). Several speedometers have been developed and experimentally calibrated to determine magma decompression rate, often utilizing fine-scale textures (e.g., bubbles, microlites) preserved in rapidly quenched

Project Administration: Behnaz Hosseini, Madison L. Myers, James M. Watkins
Resources: Madison L. Myers, James M. Watkins
Software: Behnaz Hosseini, Madison L. Myers, James M. Watkins
Supervision: Madison L. Myers, James M. Watkins
Validation: Behnaz Hosseini
Visualization: Behnaz Hosseini
Writing – original draft: Behnaz Hosseini
Writing – review & editing: Behnaz Hosseini, Madison L. Myers, James M. Watkins, Megan A. Harris

eruptive products. For example, reaction rims on hydrous minerals subjected to conditions outside of their stability fields (e.g., Rutherford & Devine, 2003; Rutherford & Hill, 1993) and the size and number density of microlites (e.g., Andrews & Befus, 2020; Castro & Gardner, 2008; Couch et al., 2003; Hammer & Rutherford, 2002; Toramaru et al., 2008) provide textural records of slower (weeks to days) magma decompression or stalling, often for dome-building phases of eruptions (e.g., Geschwind & Rutherford, 1995; Rutherford & Devine, 2003). This is largely due to the rate-limited nature of crystal nucleation, growth, and decomposition, particularly in low temperature, highly viscous rhyolitic melts, although microlite textures have also been used to infer fast decompression rates (equivalent to <1 day) for explosive rhyolitic eruptions (Andrews & Gardner, 2010; Castro & Dingwell, 2009). On the other hand, the most rapid (minutes to seconds) petrologically resolvable decompression rates are archived in the size and number density of bubbles (e.g., Hajimirza et al., 2021; Hamada et al., 2010; Mourtada-Bonnefoi & Laporte, 2004; Shea, 2017; Toramaru, 2006), and are weighted toward recording the final part of an accelerating decompression path in the shallow conduit due to the large supersaturation pressures required to achieve nucleation (Shea, 2017). All of the above are reaction speedometers, where an observed natural texture is compared to an experimental calibration under different compositional, temperature, and/or pressure conditions. In recent decades, magma ascent speedometry has benefited from the development of diffusion-based techniques to extract timescales from records of volatile (e.g., H_2O, CO_2) or elemental (e.g., Li) disequilibria preserved in melt and crystals (Costa et al., 2020). One diffusive process that can potentially record the elusive minutes- to hours-long decompression timescales not readily captured by the techniques above is the flux of volatiles (H_2O, CO_2, S, etc.) through embayments: crystal-hosted melt-filled channels that remain open to, and thus can chemically exchange with, the surrounding magma during storage and ascent (Anderson, 1991; Liu et al., 2007). During magma decompression and ascent, the solubility of volatiles dissolved in the melt lowers resulting in exsolution into a separate fluid phase. Embayment melt, when quenched to glass, preserves concentration gradients that form during decompression as volatiles that are saturated in the melt diffuse from the embayment interior into a bubble at the outlet in an attempt to maintain equilibrium with the surrounding degassing melt. Volatile concentration gradients in embayments are measured using microanalytical techniques and are forward-modeled numerically using chemical diffusion principles to estimate magma decompression rates (Liu et al., 2007).

The embayment speedometer has been leveraged in explosive eruptions spanning a broad compositional range, with studies on rhyolite to rhyo-dacite (Geshi et al., 2021; Humphreys et al., 2008; Liu et al., 2007; Myers et al., 2018, 2021; Saalfeld et al., 2022) as well as basaltic-andesite to basalt (Ferguson et al., 2016; Lloyd et al., 2014; Moussallam et al., 2019; Newcombe et al., 2020; Zuccarello et al., 2022) providing insights into how magma decompression rate may (or may not) correlate with eruption composition and explosivity (Figure 1). However, attempts to model volatile concentration gradients in embayments have seen variable success, likely a result of complex magma decompression histories being met with simplifying model assumptions (deGraffenried & Shea, 2021; Su & Huber, 2017). For example, several studies have found that embayments often preserve interior $H_2O \pm CO_2$ concentrations and corresponding saturation pressures lower than those of co-erupted melt inclusions, with the use of melt inclusion-derived storage pressures therefore in some cases unsuccessful in producing good model fits to the observed concentration gradients (Lloyd et al., 2014; Myers et al., 2018, 2021; Saalfeld et al., 2022). This has been interpreted to suggest an initial period of slow decompression that allows for re-equilibration of the embayment interiors to lower concentrations prior to more rapid decompression approaching fragmentation (Myers et al., 2018). Additionally, although equilibrium degassing during decompression is a commonly applied boundary condition in embayment modeling, prior decompression experiments have emphasized the role of delayed, disequilibrium degassing, especially in high silica rhyolitic melts (Mangan & Sisson, 2000) and recent numerical studies have revealed the significant effect that the assumption of degassing mechanism can have on calculated decompression rates (deGraffenried & Shea, 2021). Lastly, order-of-magnitude variations in decompression rates within single ashfall units have been observed, and are thought to represent variable flow in the conduit or fluctuations in ascent dynamics experienced over the course of a single eruption (Myers et al., 2018; Saalfeld et al., 2022).

In light of the ambiguity of results from studies in natural systems, embayments must be subjected to rigorous experimental evaluation in order to validate their application as robust recorders of decompression rate, and to identify the limitations of this technique. This, in turn, will allow for integration of embayment-based magma decompression rates with other independent petrologic and monitoring-based estimates for a more complete understanding of magma transport from source to surface. Controlled dynamic experiments allow for close

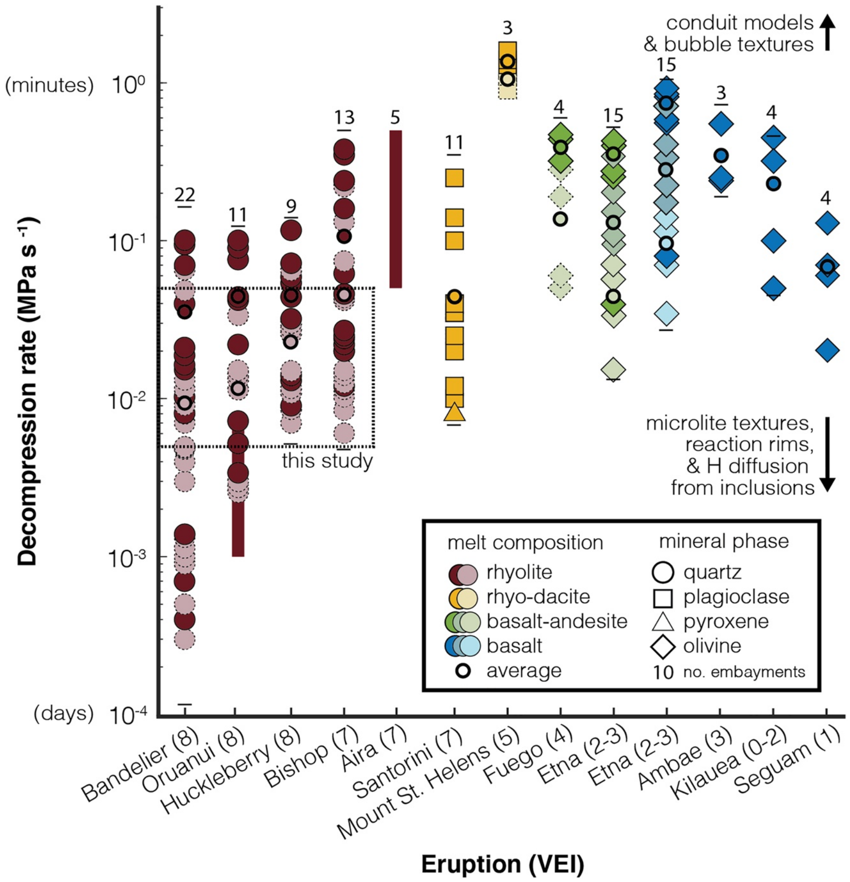

Figure 1. Compilation of embayment-based magma decompression rates for eruptions of various melt composition and magnitude (Volcanic Explosivity Index or VEI, 0–8). For Bandelier, Oruanui, Huckleberry, and Bishop, rates based on both melt inclusion (light red) and embayment interior (dark red) starting conditions are included, along with their corresponding averages. Vertical red bars represent a range of decompression rates reported for Oruanui and Aira (i.e., no discrete rates published). For Mount St. Helens, modeling results for both low (light yellow) and high (dark yellow) initial H_2O are included, along with the corresponding averages. Two-stage modeling results are included for Fuego, with an initial slow rate (light green) and a final faster rate (dark green). For Etna, the two columns represent the same data set but with different parameterizations in the modeling based on a basaltic-andesite (green) or basaltic-trachyte (blue) composition. For each, the color symbolization (light, middle, and dark green and blue) represents different eruptions of Etna (a flank eruption, a lava fountaining episode, and a paroxysmal eruption). Where available, the minimum and maximum decompression rates taking into account published errors are indicated by horizontal black bars. The number of embayments analyzed in each study are indicated at the top of each column of data. The composition and rates considered in this experimental study are indicated by the dotted square. Eruptions included are 1.61 and 1.26 Ma Bandelier (Saalfeld et al., 2022), 26.5 ka Oruanui (Liu et al., 2007; Myers et al., 2018), 2.08 Ma Huckleberry (Myers et al., 2018), 760 ka Bishop (Myers et al., 2018), 30 ka Aira (Geshi et al., 2021), 3.6 ka Santorini (Myers et al., 2021), 1980 Mount St. Helens (Humphreys et al., 2008), 1974 Fuego (Lloyd et al., 2014), 2013, 2015, and 2018 Etna (Zuccarello et al., 2022), 2018 Ambae (Moussallam et al., 2019), 1500 CE, 1600 CE, and 1959 Kilauea (Ferguson et al., 2016), and 1977 Seguam (Newcombe et al., 2020).

examination of how pressure-temperature-time ($P-T-t$) conditions in the conduit govern the kinetics of degassing and diffusion through melts (Martel et al., 2017). These experiments allow the user to impose and control several intensive variables (e.g., P, T, f_{O2}) that are usually unknown or estimated in natural systems. Such experiments have been used extensively to investigate decompression-induced bubble nucleation and growth as well as microlite crystallization (e.g., Befus & Andrews, 2018; Gardner et al., 1999; Hammer & Rutherford, 2002; Martel & Schmidt, 2003), kinetic processes that respond to the fastest and slowest segments of a magma's ascent history, respectively. In this study, we provide a similar experimental assessment of melt embayments, which are potentially the most versatile and representative petrologic recorders of magma decompression through the entire conduit for explosive eruptions.

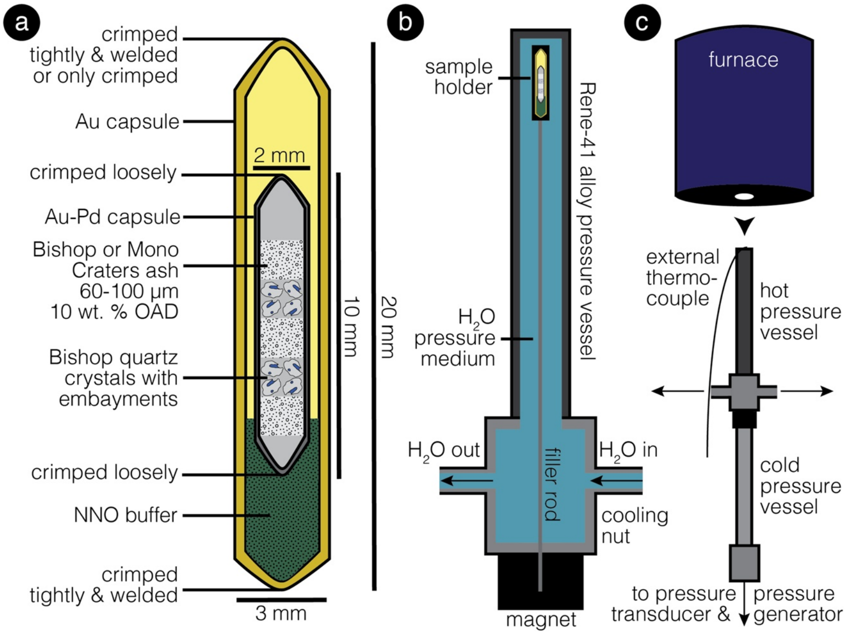

Figure 2. Schematic of (a) Au/Au-Pd double capsule loaded with embayment-bearing quartz crystals, Bishop ash with 10 wt.% OAD, and nickel-nickel oxide (NNO), (b) capsule loaded into sample holder of filler rod and into H_2O-filled Rene-41 pressure vessel and (c) assembly connected to pressure line and pressurized prior to lowering furnace. Note that the capsule is housed in the cooling nut until the pressure vessel reaches run conditions (150 MPa and 780°C).

2. Methods

2.1. High Pressure-Temperature Decompression Experiments

We developed an experimental approach to re-equilibrate natural quartz-hosted embayments at pressures (150 MPa) and temperatures (780°C) comparable to rhyolitic magma storage conditions prior to conducting controlled decompression using a cold-seal pressure vessel. The objective of these experiments is to investigate whether embayments can robustly record a range of magma decompression rates from storage to surface. Decompression rates imposed in experiments were informed by the rates estimated using quartz-hosted embayments in natural rhyolitic systems (~0.0005–0.5 MPa s^{-1}), but are confined to one order of magnitude (0.005–0.05 MPa s^{-1}) in this study (Figure 1; Myers et al., 2018; Saalfeld et al., 2022).

2.1.1. Embayment Selection and Capsule Assembly

Glass-coated quartz crystals were picked from the 500–1,000 µm size fraction of ashfall unit F9 of the 0.76 Ma Bishop Tuff, known to have abundant glass-filled embayments (Myers et al., 2018). Selected crystals were inspected with a stereo microscope for identification of glassy embayments with simple, cylindrical geometries (i.e., roughly uniform diameter from embayment interior to outlet) to justify the assumption of one-dimensional (1D) diffusion (deGraffenried & Shea, 2021). Embayments of different widths and lengths were selected in order to examine how natural variations in embayment dimensions within a single experiment might affect recovered decompression rates and/or textures (Table S2 in Supporting Information S2). Thick-walled gold (Au; outer diameter 3 mm, inner diameter 2.2 mm, length 20 mm) and gold-palladium ($Au_{75}Pd_{25}$; outer diameter 2 mm, inner diameter 1.75 mm, length 10 mm) tubes were cut and tri-crimped at one end, with Au tubes subsequently welded at the same end using a Lampert PUK 2 arc microwelder with argon as the shielding gas to prevent oxidation. Welded Au capsules were annealed in a muffle furnace at ~1,000°C and atmospheric pressure for at least 2 hr to heal microfractures. Each inner Au-Pd capsule was packed with 4–10 embayment-bearing quartz crystals and 3–10 mg of 60–100 µm Bishop or Mono Craters ash mixed with 10 wt.% oxalic acid dihydrate (OAD; $(COOH)_2 \cdot 2H_2O$), a C-O-H fluid source used to vapor-saturate the melt at the imposed initial $P - T$ conditions. The Au-Pd capsule was then loosely tri-crimped on the second end and placed in the Au capsule (i.e., double capsule technique) atop 25–50 mg of a solid nickel-nickel oxide (NNO) buffer assemblage to control redox conditions (Figure 2a). At high temperatures and in the presence of the NNO buffer, the OAD

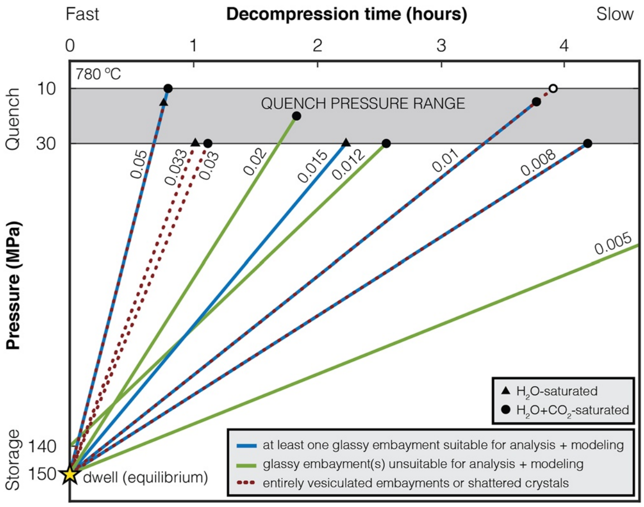

Figure 3. Imposed decompression pathways for 13 experiments, ranging from 0.005 to 0.05 MPa s^{-1}. Annotated rates are in MPa s^{-1}. All but one experiment began from storage at 150 MPa, and all quenched between 10–30 MPa. Triangles denote H_2O-saturated experiments, while circles denote $H_2O + CO_2$-saturated experiments. The open circle denotes the only experiment (E1) that was rapid H_2O-quenched. Solid blue lines represent experiments from which at least one glassy embayment was suitable for Fourier-transform infrared spectroscopy and modeling. This does not, however, preclude the presence of vesiculated embayments in these experiments. Solid green lines denote experiments from which glassy embayments recovered were unsuitable for geospeedometry due to, for example, breakage near the embayment outlet during sample preparation. Dotted red lines represent experiments in which embayments entirely vesiculated or crystals shattered. One experiment (0.008 MPa s^{-1}) was repeated three times. The slowest decompression (0.005 MPa s^{-1}) equates to 7.78 hr, while the fastest decompression (0.05 MPa s^{-1}) equates to ~45 mins.

decomposes to produce a H_2O-CO_2 fluid mixture (cf. McCubbin et al., 2014; Yoshimura & Nakamura, 2010). While the inner Au-Pd capsule was only tri-crimped to allow for interaction with the contents of the outer Au capsule, the outer Au capsule was tightly tri-crimped on the second end and either (a) welded shut to produce a mixed-volatile ($H_2O + CO_2$)-saturated system ($P_{H_2O} + P_{CO_2} = P_{TOT}$) or (b) left non-welded to produce an H_2O-saturated system ($P_{H_2O} = P_{TOT}$) (i.e., by allowing exchange with the surrounding H_2O pressurizing medium). Each double-welded capsule (charge) was weighed before and after an experiment to ensure that mass was not lost or gained during the experiment. Capsule preparation and assembly details can be found in Table S1 and Text S1 in Supporting Information S2.

2.1.2. Equilibrium and Decompression Experiments in Cold-Seal Pressure Vessel

High $P - T$ equilibrium (dwell) and decompression experiments were conducted using the vertically-oriented, externally-heated, computer-controlled, rapid-quench cold-seal pressure vessels at the University of Oregon's Experimental Geochemistry and Petrology Laboratory. These pressure vessels are H_2O-pressurized and can be operated at up to 900°C and 200 MPa, making them useful for simulating magma storage and transport conditions for more evolved, silicic systems in the uppermost crust (<8 km). Charges were loaded and secured in a bored-out Ni-alloy filler rod which was then inserted into the Rene-41 pressure vessel (i.e., autoclave; Figure 2b). The assembly was connected to a motor-controlled pressure line and pressurized to 150 ± 1 MPa at ambient temperature for at least 1 hr to confirm that the system was holding pressure. Once pressure stability was confirmed, the furnace was heated to 780°C ± 2°C and lowered over the pressure vessel while the charge was housed in the H_2O-coupled cooling nut between the hot and cold ends of the vessel. During heating, the stepper motor controlled and maintained the desired pressure. Using an external magnet, the charge was raised into the hot spot once temperature stabilized, confirmed by a temporary ~20 MPa decrease in pressure registered in the $P - T$ time-series. Each experiment began with a 24-hr dwell period to saturate and homogenize embayment melt at the imposed storage pressure, temperature, and fluid composition prior to decompression. This 24-hr dwell is based on a calculation of the time required for CO_2 to diffuse ($\tau = L^2/D$) in or out of a 200 μm melt channel at 150 MPa and 780°C in the presence of 4 wt.% H_2O (typical of natural Bishop Tuff embayments), which is on the order of 5 hr (Zhang et al., 2007). Even at the lower end of H_2O contents (~2.5–3 wt.%), the required dwell time to re-equilibrate CO_2 would be less than 20 hr. Due to the faster diffusivity of H_2O, the required dwell time to re-equilibrate H_2O at these conditions is on the order of a couple hours.

During each run, decompression followed a programmed $P - T - t$ path controlled, monitored, and recorded using LabVIEW software. Temperature and pressure were monitored continuously using a type-K (chromel-alumel) thermocouple (±2°C) positioned just above the charge in the pressure vessel and a digital Omega pressure transducer (±1 MPa) checked against a factory-calibrated Heise gauge. Two types of experiments were conducted: (a) isobaric and isothermal dwell experiments to verify re-equilibration and to confirm the equilibrium solubilities and composition of the $H_2O \pm CO_2$ fluid at storage pressures, and (b) isothermal, constant-rate, continuous decompression experiments to simulate syneruptive magma ascent and degassing and consequent diffusion through rhyolitic melt (Figure 3). Imposed decompression rates ranged from 0.005 to 0.05 MPa s^{-1}. To quench the charge, we attempted two techniques. The first was to use the rapid quench capability of the cold-seal pressure vessel, achieved by dropping the experimental charge from the hot spot into a H_2O-coupled cooling nut in 2 s. Despite the rapid quench technique being widely applied to experimental charges (e.g., Jacobs & Kerrick, 1980; Zhang et al., 2000), it resulted in shattering of crystals in our early experiments (e.g., E1) which we speculate was induced by thermal shock. To circumvent this issue, we adopted the technique of slow air quenching by raising the furnace off of the pressure vessel and allowing an isobaric quench in ambient air. A slow air quench from 780°C to below the glass transition (T_g = ~570°C) occurred in <2 min, equivalent to a cooling rate of ~1.75–2°C s^{-1} or 105–120°C min^{-1}, determined using the temperature-time series log. All experiments (except E1) ended with an isobaric air quench occurring at pressures between 10–30 MPa. The details of the experimental procedure and run conditions can be found in Table S1 and Text S1 in Supporting Information S2.

2.2. Embayment Volatile Gradient Analyses

2.2.1. Sample Preparation

Following experiments, capsules were cut at one crimped end using cutting pliers and peeled open with needle-nose pliers to recover whole glass-coated crystals, poured directly into a watch glass. Recovered quartz crystals were mounted on 1-inch round slides in Crystalbond (an acetone-soluble thermal adhesive), ensuring that the length of each embayment was oriented parallel to the slide. Each embayment was inspected to confirm the presence of a bubble at the outlet, justifying the use of the model boundary condition (i.e., equilibrium degassing; Lloyd et al., 2014). Crystals were first ground and embayments single-intersected using 1,200, 2,000, and 3,000 grit sandpaper, and then fine-polished using 6, 3, and 1 μm polishing pads with diamond compound on a lap wheel or H_2O-lubricated aluminum oxide polishing paper. Following single intersection of embayments, the slides were reheated on a hot plate at ~150°C, crystals were flipped, and using the same sequence as above, the embayments were double-intersected to produce thin wafers (~30–70 μm). Finally, the Crystalbond was dissolved in acetone to release the wafer from the slide. Once the wafers were cleaned, they were transferred to a KBr salt plate for Fourier-transform infrared (FTIR) spectroscopic analysis. Because errors in thickness can result in large uncertainties in calculated H_2O and CO_2 concentrations, wafer thicknesses were determined using interference fringes in reflection spectra collected on the host quartz near the embayment (Nichols & Wysoczanski, 2007; Wysoczanski & Tani, 2006). If cross-polarized photomicrographs indicated wafer thickness variations along the length of the embayment, reflectance measurements were taken near the embayment outlet and interior to quantify a thinning factor.

2.2.2. FTIR Analyses of Volatiles

Glass was measured for $H_2O \pm CO_2$ concentrations from the embayment interior to the outlet using the Nicolet iN10 MX infrared microscope and integrated spectrometer at Montana State University. Absorbances were measured using a liquid nitrogen-cooled MCT-A detector, Ge-coated KBr beamsplitter, transmission collection mode, spectral resolution of 4–8 cm^{-1}, 20 × 20 μm beam aperture size, 10–20 μm step size, and collection time of at least 51 s (256 scans) per spot. To reduce artifacts from atmospheric CO_2 and water vapor and to improve the signal-to-noise ratio, a purge gas generator continuously supplied purified dry CO_2-free air to the sample chamber. Absorbance peak heights for both volatile species were measured using a linear regression baseline and subsequently converted to concentration (wt.% H_2O and ppm CO_2) using the Beer-Lambert law:

$$C_i = (M_i A)/\rho d \epsilon \tag{1}$$

where the subscript i refers to each volatile species (i.e., H_2O, CO_2), C is the concentration of the absorbing species (weight fraction), M is the molecular weight of the species (g mol^{-1}), A is the measured absorbance (peak height) of the relevant vibration band (total H_2O peak at ~3,570 cm^{-1} and molecular CO_2 peak at ~2,350 cm^{-1}), ρ is the rhyolitic glass density (g L^{-1}), d is the wafer thickness (cm), and ϵ is the molar absorption coefficient (L mol^{-1} cm^{-1}). In instances where the total H_2O peak at ~3,570 cm^{-1} saturated the detector (e.g., embayments from the H_2O-saturated dwell experiment), H_2O concentrations were measured using the absorbance peak heights of bound hydroxyl (OH^-, ~4,520 cm^{-1}) and molecular H_2O (H_2O_m, ~5,230 cm^{-1}), using a linear baseline and following the equation of Zhang et al. (1997). Because ρ and ϵ are strongly dependent on H_2O concentration, initial values of 2,350 kg m^{-3} and 80 L mol^{-1} cm^{-1}, respectively, were assumed for rhyolitic glass and then a calculation was iterated through to converge upon the appropriate values (Leschik et al., 2004; Skirius et al., 1990). The ϵ for CO_2 in rhyolitic glass is 1,214 L mol^{-1} cm^{-1} (Behrens et al., 2004). Analytical uncertainties in H_2O and CO_2 concentrations for each embayment were determined by propagating error from uncertainties in the variables entered into the Beer-Lambert equation, with thickness uncertainties being the most significant contribution. The corresponding analytical errors for the presented embayments range from ±0.13–0.32 wt.% H_2O (average 0.23 wt.%) and ±15–29 ppm CO_2 (average 23 ppm). Complete FTIR transect data and uncertainties can be found in Table S3 in Supporting Information S2.

2.3. 1D Numerical Decompression-Diffusion Modeling

Measured volatile concentration gradients were modeled using a 1D decompression-diffusion model that evolves at each time-step in response to magma decompression and degassing. The governing equation for 1D time-dependent diffusion with non-constant, H_2O-dependent diffusivity is given by:

$$\frac{\partial C}{\partial t} = \frac{\partial}{\partial x}\left(D\frac{\partial C}{\partial x}\right) \tag{2}$$

where D is the diffusivity of the volatile species in silicate melt (μm^2 s^{-1}) as a function of total dissolved H_2O concentration, C is the concentration of the diffusing species in the melt (wt.%), x is distance (μm), and t is time (s). To model diffusion of volatiles through melt-filled embayments during decompression, we replace the partial derivatives in Equation 2 with forward finite-difference numerical equations in MATLAB using the method of Liu et al. (2007) adapted by Myers et al. (2018).

In our model, H_2O and CO_2 diffuse through a melt-filled embayment in response to changing volatile solubilities induced by magma decompression. The boundary condition at the bubble-melt interface is updated at each decompression time-step and is assumed to be in local equilibrium with the exsolved gas present in the melt surrounding the crystal (based on melt H_2O and CO_2 solubility at a given pressure; Liu et al., 2005). To calculate the solubility of the H_2O-CO_2 fluid, we use the empirical expression of Liu et al. (2005) for the coupled solubility of H_2O and CO_2 in a high-silica rhyolitic melt as a function of pressure (P), temperature (T), and gas composition (X). For the diffusivities (D_{H_2O} and D_{CO_2}), we use the expressions of Zhang and Behrens (2000) and Zhang et al. (2007) that describe their dependence on P, T, and, for D_{H_2O}, X. At the other end of the model domain (i.e., the melt-crystal interface) we impose a no-flux boundary condition (i.e., $\partial C/\partial x = 0$).

Model input parameters include: (a) initial dissolved volatile concentrations (C_{H_2O}; wt.% and C_{CO_2}; ppm) which are confirmed using dwell experiments; (b) starting pressure (P_i; MPa); (c) temperature (T; °C); and (d) embayment length from the interior glass-crystal interface to the glass-bubble interface (x; μm). The following parameters are treated as unknowns: (a) decompression rate (dP/dt; MPa s^{-1}), (b) final (quench) pressure (P_f; MPa), and (c) bubble radius (r; μm), which determines the vapor-melt boundary concentration of H_2O and CO_2 at each time-step and, by extension, the gradients in H_2O and CO_2 that drive diffusion into the vapor bubble. The model includes an error minimization function that cycles through the above free parameters to find the best fit, calculated using a chi-squared (χ^2) criterion (Myers et al., 2018). The code and all relevant documentation are available on GitHub and archived on Zenodo (https://zenodo.org/record/7803186).

3. Results

3.1. Experimentally Produced Embayment Textures

A notable result from the experiments is that embayments exhibit variably vesiculated textures. Of the 48 embayments recovered (out of $n \sim 100$ crystals placed into capsules), 32 preserve pristine glass, whereas the remaining 16 contain intruding bubbles, discrete internal bubbles, or are completely vesiculated (Figure 4a). Glassy embayments predominantly (>87%) range in length from 35 to 175 μm, with the remaining ∼13% preserving slightly longer lengths between 215–270 μm. For non-glassy (i.e., vesiculated) embayments, 10 (63%) have lengths between 200–400 μm, while the remaining 37% range from 90 to 150 μm (Figure 4b). Conversely, embayments spanning the entire textural spectrum have a similar range of widths—measured at the embayment outlet inbound of the bubble—from 20 to 180 μm for glassy embayments and from 40 to 150 μm for vesiculated embayments. Although there are weak relationships between length and texture, we found that several embayments with roughly the same length from the same experiment exhibit a range of textures (Figure 4a). This intra-experimental variability in embayment textures was observed in at least seven of the 15 experiments (decompression and dwell). We also found the full range of textures within an individual crystal. Finally, we note that decompression experiments conducted under nearly identical conditions (i.e., decompression rate, temperature, etc.) can produce embayment populations with vastly different textural characteristics, from entirely vesiculated to pristine dense glass or both (see results from experiments run at 0.008, 0.01, and 0.05 MPa s^{-1}; Figure 3). These results indicate that the pristine glassy textures desirable for volatile analyses cannot yet be produced by experiments in a predictable or controlled way. However, the stochastic nature of embayment textures in our experiments is commensurate with natural observations of variably vesiculated embayments within single ashfall layers or even single crystals from many silicic caldera-forming eruptions and

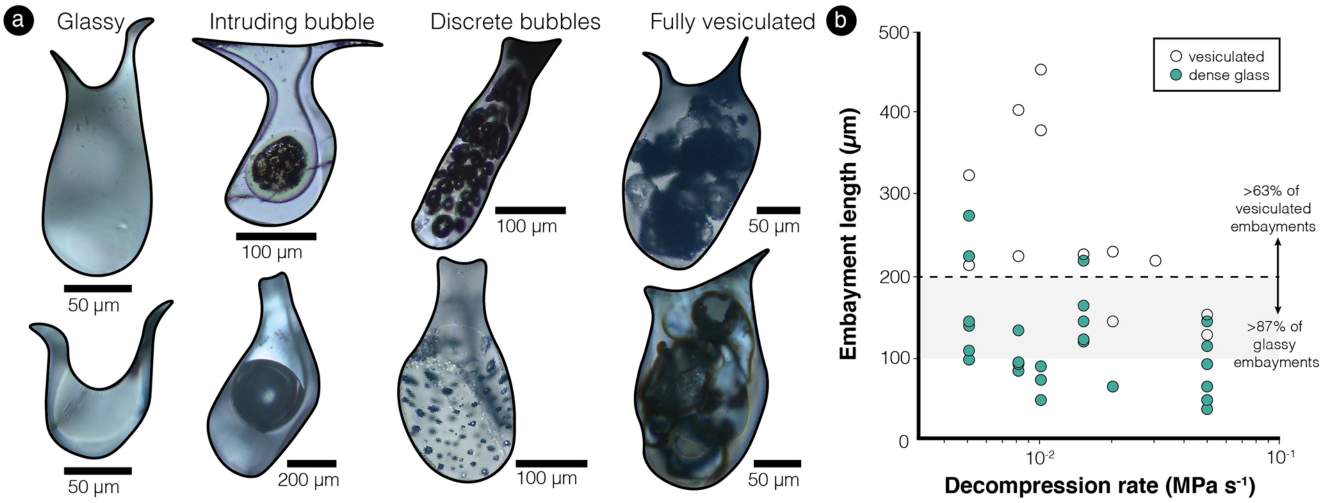

Figure 4. (a) Variety of textures produced in embayments during experiments: glassy, intruding bubble, discrete internal bubbles, and fully vesiculated. We find that a single experiment or even a single crystal can produce embayments with different textures, such as the top middle two embayments found within one crystal. (b) Embayment texture as a function of embayment length for different decompression rates. Vesiculated embayments (including those with intruding and discrete bubbles) denoted by open circles, and dense glassy embayments denoted by closed teal circles. Gray shaded region indicates the characteristic length scales (100–200 µm) suggested by Cashman and Rust (2016) as key to preserving dense glass. Our results are in general agreement with this observation, with >63% of vesiculated embayment >200 µm in length and >87% of glassy embayments <200 µm.

also suggests that these textures can be representative of the same experienced decompression history (Ruefer et al., 2021). Complete embayment dimensions and textural descriptions can be found in Table S2 in Supporting Information S2.

The results hereafter focus solely on the glassy embayments for which volatile concentration gradients could be measured. Despite our best efforts to control for embayment geometry during the selection process, recovered embayments range in shape from simple or slightly bulbous (80%) to bent or complex (15%) (Table S2 in Supporting Information S2; morphology classification of Ruefer et al., 2021).

3.2. Equilibrium (Dwell) Experiments

Dwell experiments were used to demonstrate that volatile concentrations in natural embayments could be re-equilibrated to the initial conditions of our decompression experiments. Based on H_2O and CO_2 concentrations measured in embayment interiors, the vapor composition from ashfall unit F9 of the Bishop Tuff is $X_{H_2O} \sim 0.75$ and $X_{CO_2} \sim 0.25$ in equilibrium with 4.5 wt.% H_2O and 220 ppm CO_2 dissolved in the melt at 740°C and ∼145 MPa (Myers et al., 2018). Two isothermal and isobaric dwell experiments (D1 and D2) show that embayments can re-equilibrate to the initial conditions of our experiments within 24 hr (Figure 5). The H_2O (∼2.4 wt.%) and CO_2 (∼700 ppm) concentrations from the closed-capsule, mixed-volatile dwell experiment cluster around the 150 MPa isobar, indicating that re-equilibration was achieved, and that the fluid produced by OAD decomposition is $X_{H_2O} \sim 0.30$ and $X_{CO_2} \sim 0.70$ (Figure 5; Liu et al., 2005). Additional evidence for re-equilibration in the 24-hr mixed-volatile dwell experiment comes from four points measured along a transect in one embayment (D1-1), which preserves flat H_2O and CO_2 concentration profiles (Table S3 in Supporting Information S2).

The H_2O concentrations from the open-capsule (no CO_2) dwell experiment also predominantly overlap the 150 MPa isobar but are more variable than expected, ranging from 4.88 to 5.22 wt.% H_2O (Figure 5). We do not have a satisfying explanation for this variability but can rule out insufficient time for re-equilibration for at least three reasons: (a) the FTIR transect within embayment D2-9 does not show any systematic H_2O enrichment toward the embayment outlet, as would be expected during the re-equilibration process; (b) the re-equilibration time should be shorter for this experiment compared to the closed-capsule dwell experiment due to the Bishop conditions being more similar (Figure 5); (c) the re-equilibration time should be shorter at higher H_2O contents and the embayments from the closed-capsule dwell experiment were able to re-equilibrate in the presence of significantly lower dissolved H_2O contents.

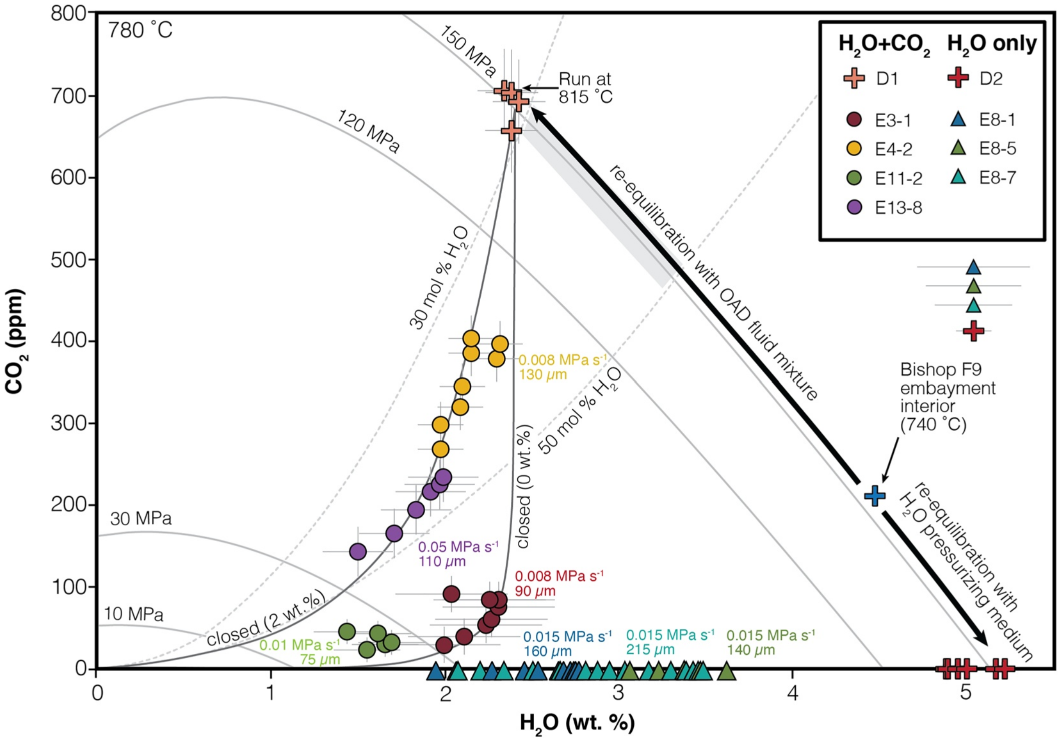

Figure 5. H_2O and CO_2 concentrations in embayments from dwell and decompression experiments. Isobars shown as solid light gray curves, degassing paths shown as solid dark gray curves from one starting fluid composition (relevant to E4-2), and fluid composition isopleths shown as dashed light gray curves, calculated using the Liu et al. (2005) solubility model. Error bars indicated as light gray lines on measured points for mixed-volatile experiments, or below legend for H_2O-only experiments. Pink and red crosses represent results from mixed-volatile (D1) and H_2O-saturated (D2) dwell experiments, respectively. Both the D1 and D2 results cluster around the 150 MPa isobar. Also shown for reference is the inferred vapor composition (75 mol% H_2O) and volatile concentrations for ashfall unit F9 of the Bishop Tuff (the starting material used in our experiments; Myers et al., 2018). Shaded light gray region denotes the range in fluid composition (30–50 mol% H_2O) required to successfully model measured profiles in embayments from mixed-volatile experiments. Circles represent results from mixed-volatile experiments, while triangles represent results from H_2O-saturated experiments. Each color represents volatile concentrations measured within a single embayment. We note that D1 was run at a slightly higher temperature (815°C) than all other experiments, but has overall negligible effects on calculated H_2O and CO_2 contents so is included on the same plot for clarity.

3.3. Decompression Experiments

We use the following criteria to describe the outcome of each of the decompression experiments: (a) an effective experiment produced at least one glassy embayment suitable for analysis and modeling, and (b) an ineffective experiment produced no usable embayments, usually due to crystal shattering or complete vesiculation of embayments, or glassy embayments unsuitable for speedometry (e.g., poor volatile constraints at their outlets due to breakage). Hereafter, we present analytical and modeling data for embayments from effective experiments only. All measured embayment volatile concentrations are reported in Table S3 in Supporting Information S2.

3.3.1. H_2O-Saturated

Of the four H_2O-saturated decompression experiment runs, one (E8, decompressed at 0.015 MPa s^{-1}) produced usable, glassy embayments. Two other experiments (E2 and E9) that underwent faster decompression (0.033 and 0.05 MPa s^{-1}) yielded entirely shattered crystals or vesiculated embayments. As expected due to the slower decompression (0.005 MPa s^{-1}), E10 embayments preserved systematically lower H_2O concentrations (1–2 wt.%) and flatter concentration profiles than E8 embayments; however, none of the embayments from this experiment met the criteria for diffusion modeling (i.e., poor volatile constraints at outlet). Six glassy embayments were recovered from E8, with three (E8-1, -5, -7) successfully analyzed for H_2O concentration gradients that range from ~2.8–3.6 wt.% in the interiors and ~2–3 wt.% at the outlets (Figure 6; Table 1).

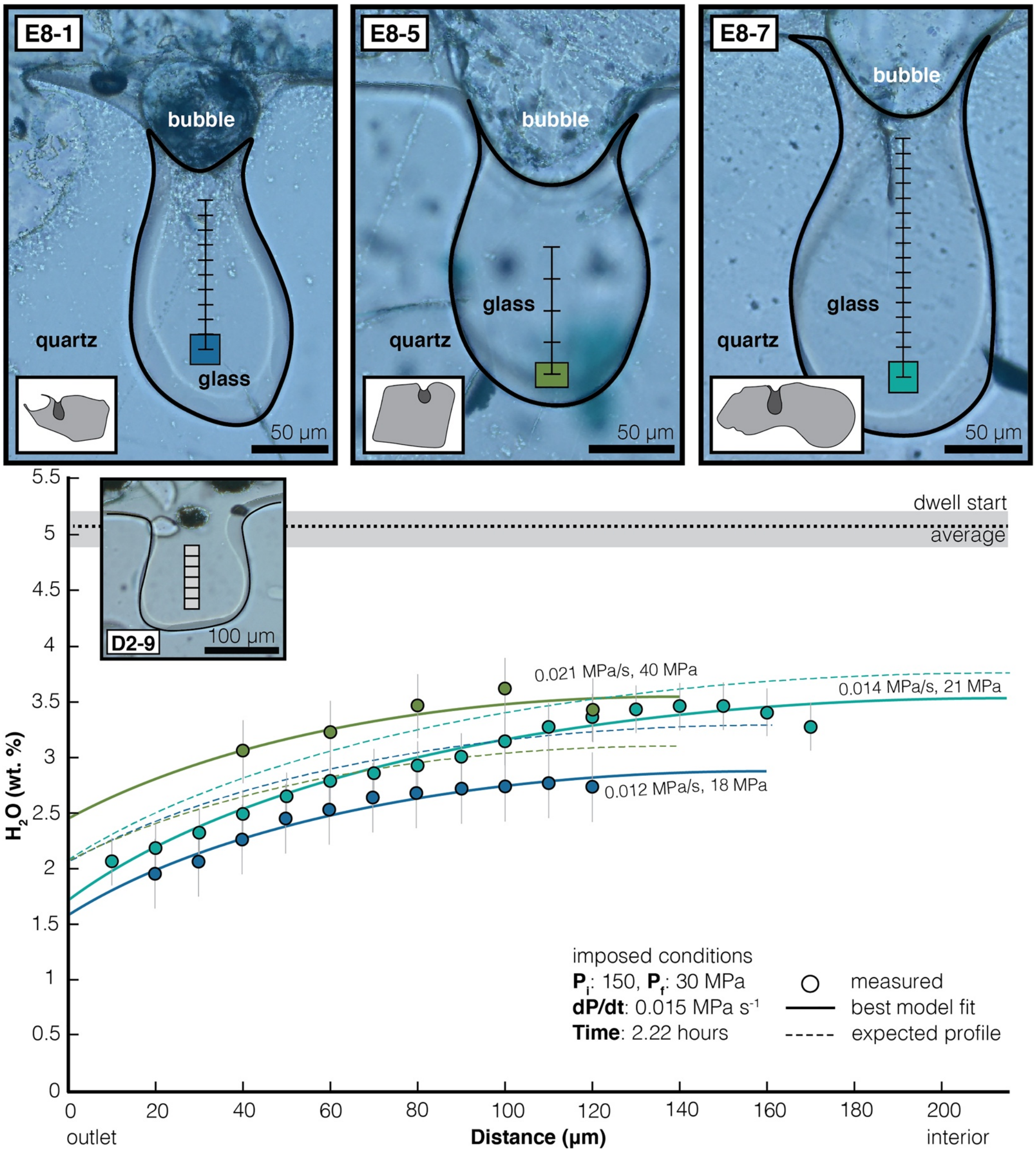

Figure 6. Three glassy embayments recovered from E8 (H_2O-saturated) with measured transects indicated on each. E8-1, -5, and -7 modeled profiles retrieve a range of decompression rates (0.012–0.021 MPa s^{-1}) that closely bracket the known rate (0.015 MPa s^{-1}). Colored box on each embayment represents the beam aperture (either 15 × 20 or 20 × 20 μm). Insets show the size and location of each embayment relative to the host quartz. Range of initial H_2O concentrations measured in embayment D2-9 (solid gray region) along with the average value used in modeling profiles (dotted black line) are indicated on plot. Measured H_2O concentration gradients (circles) for each of the three embayments are shown along with expected profiles (dashed lines) and best model fits (solid lines). Error bars on each measured point are shown in light gray.

Overall, the modeled gradients in E8 embayments are in good agreement with the expected profiles (Figure 6). The best-fit decompression rates range from 0.012 to 0.021 MPa s^{-1} (Table 2). These values closely bracket the known decompression rate (0.015 MPa s^{-1}) and thus do not seem to be noticeably affected by the 25–43% necked geometries of these embayments. The modeled quench pressures for the E8 profiles are somewhat variable (18–40 MPa), owing to variability in H_2O near the outlets, but these values also bracket the known quench pressure (30 MPa). If we fix the quench pressure in the model runs to that imposed during the experiment (30 MPa), we recover best-fit decompression rates spanning a wider range, from 0.006 to 0.029 MPa s^{-1} with consistently higher χ^2 values (i.e., poorer fits) (Table S4 in Supporting Information S2). These recovered decompression rates are 0.4–2 times the imposed rate (0.015 MPa s^{-1}), compared to 0.8–1.4 when we allow quench pressure to vary as a free parameter.

Table 1
Experimental Conditions and Fourier-Transform Infrared Spectroscopy Results

ID	Length (μm)	Imposed conditions Temperature (°C)	Decompression rate (MPa s^{-1})	Quench pressure (MPa)	Ascent time (hours)	Dwell H_2O (wt.%)	CO_2 (ppm)	Pressure (MPa)	Embayment interior H_2O (wt.%)	CO_2 (ppm)	Pressure (MPa)	Embayment outlet H_2O (wt.%)	CO_2 (ppm)	Pressure (MPa)	H_2O error (wt.%)	CO_2 error (ppm)
E8-1[a]	160	780	0.015	30	2.22	5.1	0	150	2.77	0	51	1.95	0	26	0.32	–
E8-5[a]	140	780	0.015	30	2.22	5.1	0	150	3.62	0	81	3.06	0	60	0.27	–
E8-7[a]	215	780	0.015	30	2.22	5.1	0	150	3.48	0	75	2.07	0	30	0.22	–
E3-1[b]	90	780	0.008	30	4.17	3	550	150	2.33	82	50	2.01	27	32	0.32	22
E4-2[b]	130	780	0.008	30	4.17	2.4	690	150	2.34	399	102	2	271	71	0.13	28
E11-2[b]	75	780	0.01	15	3.75	3	550	150	1.61	45	26	1.55	25	22	0.19	15
E13-8[b]	110	780	0.05	10	0.78	3.5	430	150	1.98	235	65	1.49	142	40	0.20	29

[a]H_2O-saturated experiment. [b]$H_2O + CO_2$-saturated experiment.

3.3.2. Mixed-Volatile ($H_2O + CO_2$)-Saturated

Four (E3, E4, E11, E13) of nine mixed-volatile experiments were effective, with imposed decompression rates spanning nearly an order of magnitude (0.008–0.05 MPa s^{-1}). Foremost, we find that using the estimated mixed-volatile composition from dwell experiment D1 (~2.4 wt.% H_2O and ~700 ppm CO_2) as initial conditions results in good model fits for all measured H_2O profiles; however, the model consistently underestimates the extent of CO_2 diffusion observed (except for E4-2). We tentatively attribute this persistent issue to vapor bubbles within the experimental charge having different compositions along the starting pressure isobar, as opposed to the diffusivity of CO_2 being underestimated (see discussion for full reasoning). This variable OAD breakdown hypothesis is supported by improved model fits when we allow the initial fluid composition to vary along the starting pressure isobar (150 MPa) between ~2.4–3.5 wt.% H_2O. For instance, in E3 and E4, two embayments (E3-1 and E4-2) preserve comparable volatile concentration gradients, with similar H_2O (~2.3 wt.%) but vastly different CO_2 concentrations (~80 vs. 400 ppm) (Figures 7a and 7b; Table 1). Given that these embayments experienced the same decompression pathway and have overall similar lengths, the five-fold difference in CO_2 concentrations suggests that they started with different fluid compositions at 150 MPa (~30 vs. 40 mol% H_2O). Indeed, we can fit E3-1 volatile profiles using a starting H_2O concentration of 3 wt.%, while E4-2 is best fit using 2.4 wt.% (the result from dwell experiment D1) (Figures 7a and 7b). This results in recovered decompression rates of 0.008 (E3-1) and 0.006 (E4-2) MPa s^{-1}, in excellent agreement with the known rate (0.008 MPa s^{-1}) (Table 2).

Two faster mixed-volatile decompression experiments (E11 and E13) each yielded one usable glassy embayment. E11-2 exhibits relatively flat concentration profiles for both H_2O (~1.5–1.6 wt.%) and CO_2 (~25–45 ppm) (Figure 7c; Table 1). Using a 3 wt.% H_2O and 550 ppm CO_2 starting condition, we recover a best-fit decompression rate of 0.009 MPa s^{-1} and a quench pressure of 14 MPa, close to the imposed rate (0.01 MPa s^{-1}) and quench pressure (15 MPa) (Table 2). From the fastest decompression experiment conducted, E13-8 preserves the most pronounced H_2O concentration gradient (~1.5–2 wt.%) of the mixed-volatile experiments (Figure 7d; Table 1). Using a starting condition of 3.5 wt.% H_2O and 430 ppm CO_2, the best-fit model for E13-8 yields a decompression rate (0.031 MPa s^{-1}) and quench pressure (5 MPa), which differ by a factor of 1.6–2 from the imposed conditions (0.05 MPa s^{-1} and 10 MPa) (Table 2). For all four embayments, if we fix the quench pressure in the model runs to those imposed during the experiments (10–30 MPa), we recover best-fit decompression rates ranging from 0.008 to 0.036 MPa s^{-1}, a factor of 0.7–1.1 times the imposed rates. Although these runs have consistently higher χ^2 values, they retrieve decompression rates equal or closer to the imposed rates compared to the model runs where quench pressure varies as a free parameter (0.6–1 times the imposed rate) (Table S4 in Supporting Information S2).

3.4. Evaluating the Embayment Interior Starting Condition

Natural embayments have previously been modeled using two end-member starting conditions: the melt inclusion inferred storage pressure, as presented above, or the pressure inferred from volatile concentrations in the embayment interior (e.g., Myers et al., 2018). Although we know the experimental embayments began at 150 MPa and have partially equilibrated to lower interior pressures (<100 MPa) during decompression, here we demonstrate how modeling embayments from both mixed-volatile and H_2O-saturated experiments using the embayment interior concentrations as the starting condition can yield misleadingly fast decompression rates compared to those imposed with similarly good or better model fits.

All embayments from H_2O-saturated experiments could be successfully modeled using either the dwell (150 MPa) or embayment interior (17–81 MPa) saturation pressures, calculated using VESIcal (v.1.2.4; Iacovino et al., 2021) with the solubility model of Liu et al. (2005). Modeling the gradients in E8 embayments using their respective interior saturation pressures and assuming initially flat profiles, we recover best-fit decompression rates ranging from 0.035 to 0.071 MPa s^{-1}, a factor of 2.5–5.5 greater than those calculated using the dwell starting

Table 2

Modeling Results for H_2O- and $H_2O + CO_2$-Saturated Decompression Experiments Using Dwell and Embayment Interior Starting Conditions

	Dwell start				Embayment interior start			
ID	Decompression rate (MPa s^{-1})	Quench pressure (MPa)	Ascent time (hours)	χ^2	Decompression rate (MPa s^{-1})	Quench pressure (MPa)	Ascent time (hours)	χ^2
E8-1[a]	0.012	18	3.06	0.03	0.067	7	0.18	0.09
E8-5[a]	0.021	40	1.46	0.18	0.071	28	0.09	0.14
E8-7[a]	0.014	21	2.56	0.13	0.035	17	0.46	0.23
E3-1[b]	0.008	29	4.20	0.17	0.023	28	1.47	0.17
E4-2[b]	0.006	45	4.86	1.39	0.052	9	0.75	0.56
E11-2[b]	0.009	14	4.20	0.37	–	–	–	–
E13-8[b]	0.031	5	1.30	0.82	0.062	7	0.64	0.15

[a]H_2O-saturated experiment. [b]$H_2O + CO_2$-saturated experiment.

condition (0.012–0.021 MPa s^{-1}) (Table 2; Figure 8). This translates to ascent times from 5 to 30 min compared to 1.5–3 hr for the dwell start (Table 2). Recovered χ^2 best-fits using embayment interior starting conditions (0.04–0.23) span a similar range as those using the dwell starting condition (0.03–0.18) for E8 embayments. The results from E8 reveal how different starting conditions (e.g., melt inclusion vs. embayment interior) can yield contrasting decompression rates and ascent times with similarly good model fits. Applying the same approach to the mixed-volatile experiments, we find overall similar results (recovered decompression rates and ascent times faster by a factor of 2.5–5.5) with a notable difference being the overall better fits (0.15–0.56) to profiles using the embayment interior saturation pressures compared to the dwell start (0.17–1.39) (Table 2). This finding highlights both the importance and difficulty of choosing the most appropriate starting condition in natural systems.

4. Discussion

4.1. Experimental Successes and Challenges

Our experiments proved largely successful in (a) producing the range of textures observed in natural embayments, (b) re-equilibrating natural embayment melt to new starting fluid compositions, (c) inducing, via controlled decompression, diffusion of volatiles through embayment melt channels, (d) recovering embayments subjected to experimental conditions, and (e) inferring the experimental decompression rates using existing numerical models of decompression and diffusion. Although the recovery of embayment-bearing crystals is moderate (~50%) owing to the challenges of removing crystals from compressed capsules, if we consider only the experiments in which outer capsules were left non-welded, our crystal recovery rate is closer to ~62% compared to ~34% for closed-capsule, mixed-volatile experiments. We note two challenges with our current experimental approach: (a) uncertainty in the initial fluid composition along the starting pressure isobar for mixed-volatile experiments and, potentially less crucial, (b) constraining the quench pressure from the embayment outlets. We discuss the implications of both of these challenges below, along with possible solutions.

Although in all four mixed-volatile embayments presented here we recover visually good fits to the H_2O concentration profiles using the dwell experiment (D1) starting condition (~2.4 wt.% H_2O and ~700 ppm CO_2), as noted previously, we found that CO_2 concentrations are generally lower than expected (Figure 7). One possibility we mentioned is that the CO_2 diffusivity of Zhang et al. (2007) is underestimated. However, this is an unlikely explanation for at least two reasons. First, the diffusivity of CO_2 has been characterized across a broad range of melt compositions, including rhyolite, and the composition-dependence is weak. Thus, the expressions should be applicable to our melt composition. Second, the H_2O concentration-dependence is also well-characterized, and the diffusivity of CO_2 would have to increase with decreasing H_2O content to explain our data, which is in direct contrast with previous work (Zhang & Ni, 2010). An alternative hypothesis, which was applied above and is presented in Figures 5 and 7, is that the decomposition of the OAD is incongruent and produces a fluid composition that varies somewhat between and/or within experiments. For example, it is possible that the vapor and melt were not fully equilibrated at the onset of decompression. While the 24-hr dwell should be sufficient to equilibrate a ~100 μm embayment with a bubble at the mouth, if bubble spacing throughout the capsule is

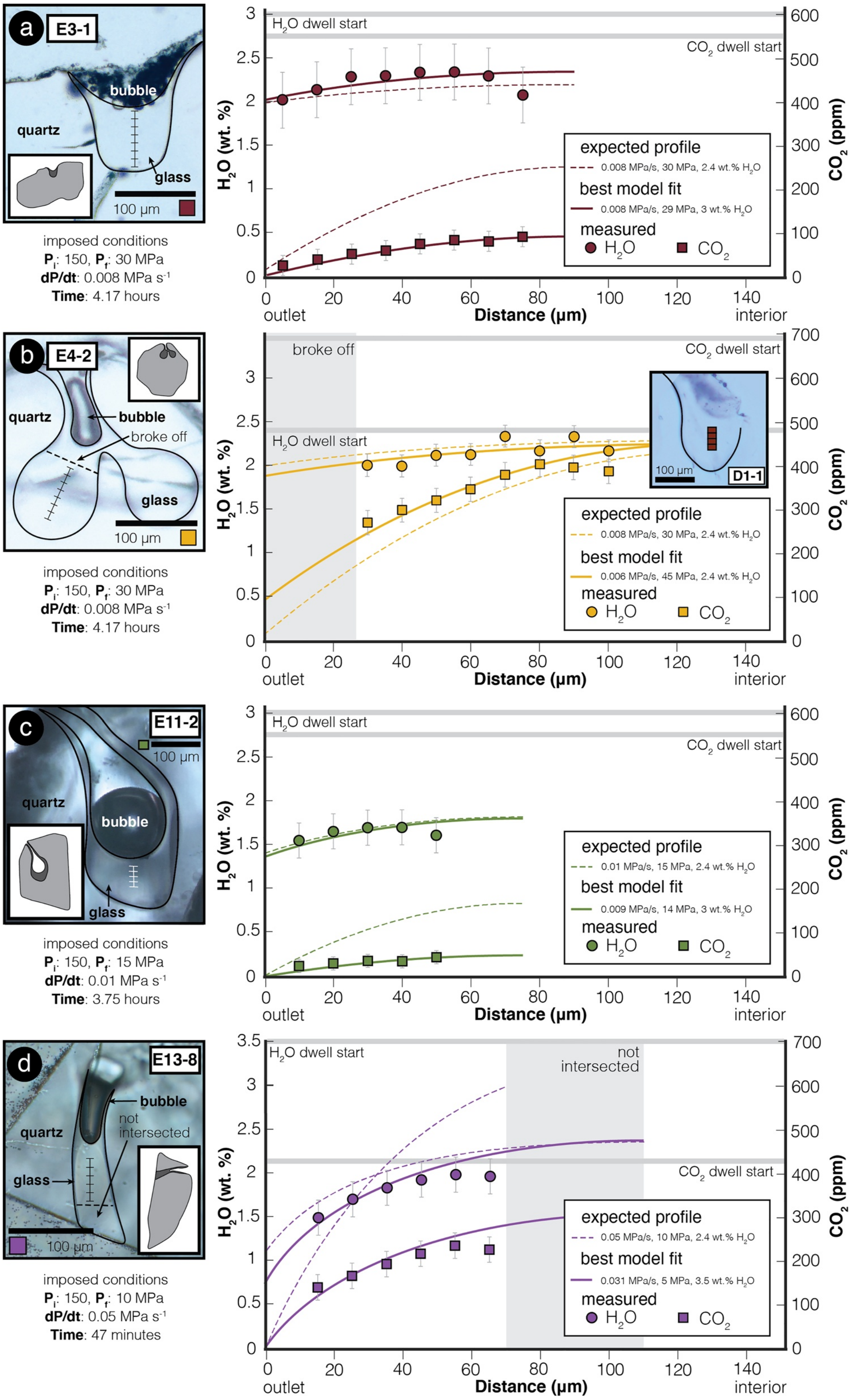
a
E3-1
bubble
quartz
glass
100 μm
imposed conditions
P_i: 150, P_f: 30 MPa
dP/dt: 0.008 MPa s^{-1}
Time: 4.17 hours
H_2O dwell start
CO_2 dwell start
expected profile
0.008 MPa/s, 30 MPa, 2.4 wt.% H_2O
best model fit
0.008 MPa/s, 29 MPa, 3 wt.% H_2O
measured
● H_2O ■ CO_2
H_2O (wt. %)
CO_2 (ppm)
Distance (μm)
outlet
interior
b
E4-2
quartz
bubble
broke off
glass
100 μm
D1-1
imposed conditions
P_i: 150, P_f: 30 MPa
dP/dt: 0.008 MPa s^{-1}
Time: 4.17 hours
broke off
H_2O dwell start
CO_2 dwell start
expected profile
0.008 MPa/s, 30 MPa, 2.4 wt.% H_2O
best model fit
0.006 MPa/s, 45 MPa, 2.4 wt.% H_2O
measured
● H_2O ■ CO_2
c
E11-2
100 μm
quartz
bubble
glass
imposed conditions
P_i: 150, P_f: 15 MPa
dP/dt: 0.01 MPa s^{-1}
Time: 3.75 hours
H_2O dwell start
CO_2 dwell start
expected profile
0.01 MPa/s, 15 MPa, 2.4 wt.% H_2O
best model fit
0.009 MPa/s, 14 MPa, 3 wt.% H_2O
measured
● H_2O ■ CO_2
d
E13-8
bubble
quartz
not intersected
glass
100 μm
imposed conditions
P_i: 150, P_f: 10 MPa
dP/dt: 0.05 MPa s^{-1}
Time: 47 minutes
H_2O dwell start
not intersected
CO_2 dwell start
expected profile
0.05 MPa/s, 10 MPa, 2.4 wt.% H_2O
best model fit
0.031 MPa/s, 5 MPa, 3.5 wt.% H_2O
measured
● H_2O ■ CO_2
0 20 40 60 80 100 120 140
0 0.5 1 1.5 2 2.5 3 3.5
0 100 200 300 400 500 600 700

Figure 7.

substantially greater than 100 μm, it is possible to have bubbles with different vapor compositions throughout the experimental charge. From our model, we find that variability in the vapor composition of the embayment bubbles ranging from 30 to 50 mol% H_2O (~2.4–3.5 wt.% H_2O) can explain the more relaxed CO_2 diffusion profiles. This hypothesis could be assessed by conducting experiments with a longer pre-decompression dwell time but crystallization within the embayment becomes a concern.

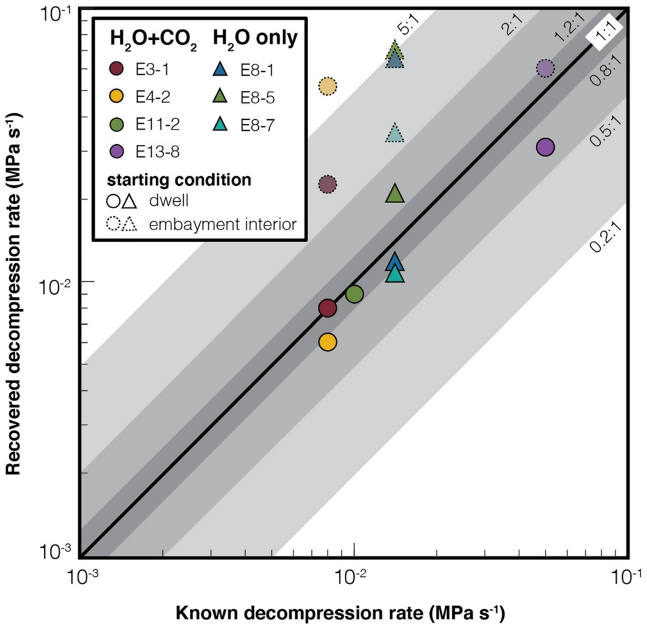

Figure 8. Known versus recovered decompression rates for the seven embayments presented in Figures 6 and 7 showing overall good agreement. The best-fit recovered decompression rates based on embayment interior starting conditions are faster (by up to a factor of 5) because less time for diffusion is needed to fit the measured profiles.

The other issue is that the model quench pressures match the known value (within 2 MPa) for only two of the seven successfully modeled embayments. For the embayments that require a lower or higher quench pressure, one reason might be the quenching process. We found that rapid H_2O quenching of experimental charges resulted in completely shattered crystals and vesiculated embayments (e.g., E1) and we therefore adopted a slow quench technique. This slow air quench, however, might be problematic in a number of ways. For one, resorption of bubbles during slow cooling can result in H_2O enrichment in the glass surrounding the bubble (McIntosh et al., 2014; Watkins et al., 2012). If this were occurring, the final pressure preserved at the embayment outlet would be higher than the true quench pressure and there would be evidence for a reverse volatile gradient inbound of the bubble. Our measurements do not resolve any H_2O enrichment just inbound of the bubble in any embayments, let alone the one that seems to require a higher quench pressure (E4-2). Another potential issue is continued volatile diffusion during slow cooling, which could alter volatile concentrations near the embayment outlet. In our experiments, a slow air quench resulted in a cooling rate of 1.75–2°C s^{-1} from ~780°C through the glass transition (T_g = ~570°C), meaning a cooling time of <2 min. This corresponds to a diffusion length of ~5–20 μm for H_2O, which is less than the spatial resolution of our measurements. We instead attribute the discrepancy between imposed and recovered (best-fit) quench pressures to wafer thickness uncertainties that translate to up- or down-shifted volatile concentration profiles. In fact, for all five embayments for which we do not recover the imposed quench pressure, the known quench pressure is within the uncertainty envelope, largely representing thickness variations, of each profile (Figures 6 and 7). Importantly, while these discrepancies in recovered outlet pressures appear to have negligible effects on recovered decompression rates, they do affect calculated ascent times, highlighting the importance of narrowly constraining wafer thickness for successful embayment studies.

4.2. The Fidelity of Embayments as Recorders of Magma Decompression

Our experiments instill confidence in the use of embayments for inferring magma decompression over a range of rates (0.008–0.05 MPa s^{-1}) and fluid compositions (pure H_2O and $H_2O + CO_2$) relevant to natural systems. Overall, all seven modeled embayments returned close to the imposed conditions. One experiment in particular (E8), where three embayments have overall similar lengths (140–215 μm) and geometries (simple to bulbous, 25%–43% necked) and recover the same experienced decompression path, attests to the reproducibility of results. We note that these embayments meet the criteria that have previously been proposed for successful embayment geospeedometry studies, with the assumption of 1D diffusion: each preserves a distinct bubble at the outlet (Lloyd et al., 2014), is necked less than ~40% (deGraffenried & Shea, 2021), and two of the three (E8-1 and E8-7) have good volatile concentration constraints within ~40 μm of the outlet (Lloyd et al., 2014) Conversely, attempts to model the H_2O profile in an embayment (E10-2) from another H_2O-saturated experiment resulted in underestimation of the known decompression rate (0.005 MPa s^{-1}) by a factor of five (0.001 MPa s^{-1}) (Table S4 in Supporting Information S2; Figure S1 in Supporting Information S1). This disagreement can be rationalized by noting that this particular embayment has a string of bubbles parallel to the diffusion profile that may have allowed H_2O to escape from the melt more efficiently

Figure 7. Four glassy embayments recovered from mixed-volatile experiments E3, E4, E11, and E13, with measured transects indicated on each. Colored box in each photo represents the beam aperture (20 × 20 μm). Insets show the size and location of each embayment relative to the host quartz. Measured H_2O (circles) and CO_2 (squares) concentration gradients for each of the embayments are shown, as well as best model fits (solid lines). Note that the expected model fits (dashed lines) based on the dwell experiment initial conditions (D1-1; ~2.4 wt.% H_2O and ~700 ppm CO_2) only provide reasonable fits to H_2O and CO_2 profiles in (b) E4-2. The other three (a, c, d) require slightly variable starting conditions in order to best-fit the measured profiles. Error bars on each measured point are indicated in light gray.

than is possible to account for with the simplified 1D model setup (Figure S1 in Supporting Information S1). Based on these results, for successful embayment geospeedometry studies using a 1D decompression-diffusion modeling approach, we emphasize the importance of selecting embayments that cohere with model assumptions (e.g., dense glass, low necking ratio, etc.) and, if possible, constraining volatile concentrations near the delicate embayment outlet. Overall, we find that embayments can, in most cases, record the imposed decompression history, and the model can retrieve this information. In scenarios where a good model fit cannot be achieved in a natural embayment, where all criteria have seemingly been met, we argue that a more complex decompression history was likely experienced, and currently cannot be extracted using a constant-rate decompression model.

Finally, while pristine glass is a prerequisite for using embayments for speedometry applications, natural and experimental embayments are characteristically multi-phased, revealing a range of textures from glassy to vesiculated (Ruefer et al., 2021). These embayment textures appear to be independent of decompression rate and the texture of the near-field matrix glass, and their intra-experimental or even intra-crystal coexistence with glassy embayments suggests some embayment-specific condition, like the existence of nanolites, is controlling their development (Shea, 2017). In our experiments, vesiculation and intruding bubbles appear most commonly in embayments longer than 200 μm (Figure 4b). Previous studies have argued for a characteristic length scale of embayments (100–200 μm) that leads to the preservation of pristine glass (e.g., Cashman & Rust, 2016), which is consistent with our results.

4.3. Experimental Insights Into Existing Magma Decompression Rate Estimates for Silicic Eruptions

Quartz-hosted embayments have been leveraged in silicic-caldera forming eruptions to estimate magma decompression rates spanning three orders of magnitude (~0.0005–0.5 MPa s^{-1}), with average rates from 0.01 to 0.1 MPa s^{-1} (e.g., Myers et al., 2018; Saalfeld et al., 2022). In some cases, these order-of-magnitude variations occur within discrete, co-erupted ashfall units (e.g., Myers et al., 2018; Saalfeld et al., 2022). These variations in decompression rate might be expected during large, dynamic eruptions where fluctuations and lateral decompression gradients can result from magma interaction with the conduit walls (Melnik & Sparks, 1999). However, it has been unclear whether the heterogeneity in decompression rates preserved within single ashfall layers is reflective of natural decompression variations in the conduit, or a result of the infidelity of embayments to record the decompression path consistently. Although we cannot necessarily scale the consistency of our experimental results up to complex natural systems, we can affirm that glassy embayments that have experienced the same decompression path can record that information with consistency. Although applying this technique to, and interpreting results from, large dynamic systems is challenging, our results suggest that crystals that have experienced the same decompression path should faithfully preserve this in the recovered glassy embayment population, as observed for embayments from discrete ashfall layers from the Late Bronze Age eruption of Santorini (Myers et al., 2021). With this in mind, when extreme decompression rate variability is recovered within individual ashfall layers or pyroclasts, it could indicate that individual crystals have observed unique decompression histories (i.e., recycling, re-equilibration during stalling in the conduit, etc.).

Our experiments span an order of magnitude of decompression rates (0.005–0.05 MPa s^{-1}) that are within the range of natural systems. However, there are additional decompression scenarios that warrant future experimentation. For instance, we did not attempt multi-day experiments to simulate the slowest recovered decompression rates from natural systems (i.e., 5.5 days in the Guaje bedded ashfall of the Bandelier Tuff; Saalfeld et al., 2022) due to challenges with controlling such slow decompression. Similarly, we did not conduct decompression experiments equivalent to the fastest ascent times recovered in natural systems (i.e., on the order of tens of minutes for 100–200 MPa pressure drops for Aira and Bishop; Geshi et al., 2021; Myers et al., 2018) because the concentration gradients will require higher spatial resolution measurements (e.g., synchrotron FTIR). In addition, in many systems, magma is inferred to undergo accelerated decompression due to an increased volume fraction of exsolved volatiles and therefore increased magma buoyancy and overpressure (Mastin, 2005) and/or to experience periods of stalling during ascent (Zimmer et al., 2007). We view the exploration of these more complex decompression scenarios as an important next step in further development of the embayment speedometer.

5. Concluding Remarks

Our experimental results build upon previous efforts to develop the application of embayments as recorders of magma decompression rate. The major findings are as follows:

1. Of the 48 embayments recovered, the majority (67%) preserve pristine glass, with the remainder compromised by intruding bubbles, discrete internal bubbles, or complete vesiculation. While this range of embayment

textures has been documented in natural silicic systems, we find no discernible correlation with decompression rate or volatile saturation state.

2. Both H_2O-saturated and mixed-volatile dwell experiments demonstrate that existing, natural embayment melt can be re-equilibrated by inward diffusion of volatiles.
3. In both H_2O-saturated and mixed-volatile decompression experiments, we find that embayments reliably record their experienced decompression pathways within the range 0.008–0.05 MPa s^{-1}.
4. Our mixed-volatile decompression experiments suggest incongruent breakdown of the OAD material and the generation of bubbles in the matrix melt with somewhat variable vapor compositions.
5. The necking geometries of successfully modeled embayments were equal to or less than what has been considered the critical degree of necking (~40%) for a 1D model approach. This adds confidence to the notion that even less-than-ideal embayments can be useful as speedometers.
6. Using embayment interior concentrations instead of the known experimental starting concentrations as initial conditions can produce misleadingly better fits to the measured profiles. For natural embayments, it remains equivocal whether co-erupted melt inclusions or interior embayment concentrations represent more accurate starting conditions, although the recovered rates and calculated times can be dramatically different.
7. There are issues that we have to contend with in the experiments that we do not have to contend with in natural samples. These include uncertainty in the starting vapor composition along the isobar and dealing with limited sample options, requiring utilization of broken or partial embayments as well as variably necked embayments. We can be more selective when picking natural embayments that cohere with the 1D modeling approach.

In this study we focused on confirming the fidelity of embayments to record constant-rate decompression scenarios using a 1D numerical modeling approach. Not accounting for the nonlinearity in magma decompression in numerical modeling of embayment diffusion profiles may result in underestimated ascent times (Su & Huber, 2017). Additionally, stalling of viscous magma (e.g., Zimmer et al., 2007) may allow time for volatile re-equilibration in embayments and, if unaccounted for, can lead to misleading decompression rate and ascent time estimates. Thus, future avenues for experimental and numerical research on embayment speedometry include (a) stalled and multi-stage decompression experiments and (b) updated numerical models to evaluate more realistic and complex decompression scenarios.

Conflict of Interest

The authors declare no conflicts of interest relevant to this study.

Data Availability Statement

All data associated with this study are presented in this paper or otherwise available in the Supporting Information S1 and S2. The 1D numerical decompression-diffusion model used in this study is publicly available and hosted on GitHub and archived on Zenodo (https://zenodo.org/record/7803186) and archived on Zenodo (https://doi.org/10.5281/zenodo.7803186). All experimental and geochemical data are available at EarthChem Library (ECL) (https://doi.org/10.26022/IEDA/112852).

Acknowledgments
B.H. acknowledges support from the Mineralogical Society of America's Grant for Student Research in Mineralogy and Petrology and the Geological Society of America's Graduate Student Research Grant, as well as National Science Foundation EAR Award 1922513 to M.L.M. The authors thank two anonymous reviewers and Benjamin J. Andrews for thorough and constructive reviews that greatly improved this publication, and Marie Edmonds for editorial handling.

References

Anderson, A. T. (1991). Hourglass inclusions: Theory and application to the Bishop Rhyolitic Tuff. *American Mineralogist*, *76*(3), 530–547.

Andrews, B. J., & Befus, K. S. (2020). Supersaturation nucleation and growth of Plagioclase: A numerical model of decompression-induced crystallization. *Contributions to Mineralogy and Petrology*, *175*(3), 23. https://doi.org/10.1007/s00410-020-1660-9

Andrews, B. J., & Gardner, J. E. (2010). Effects of caldera collapse on magma decompression rate: An example from the 1800 14C yrBP eruption of Ksudach Volcano, Kamchatka, Russia. *Journal of Volcanology and Geothermal Research*, *198*(1–2), 205–216. https://doi.org/10.1016/j.jvolgeores.2010.08.021

Befus, K. S., & Andrews, B. J. (2018). Crystal nucleation and growth produced by continuous decompression of Pinatubo magma. *Contributions to Mineralogy and Petrology*, *173*(11), 92. https://doi.org/10.1007/s00410-018-1519-5

Behrens, H., Zhang, Y., & Xu, Z. (2004). H_2O diffusion in dacitic and andesitic melts. *Geochimica et Cosmochimica Acta*, *68*(24), 5139–5150. https://doi.org/10.1016/j.gca.2004.07.008

Cashman, K. V., & Rust, A. (2016). Causes and implications of suppressed vesiculation and crystallization in phenocryst embayments.

Cassidy, M., Manga, M., Cashman, K., & Bachmann, O. (2018). Controls on explosive-effusive volcanic eruption styles. *Nature Communications*, *9*(1), 1–16. https://doi.org/10.1038/s41467-018-05293-3

Castro, J. M., & Dingwell, D. B. (2009). Rapid ascent of rhyolitic magma at Chaitén volcano, Chile. *Nature*, *461*(7265), 780–783. https://doi.org/10.1038/nature08458

Castro, J. M., & Gardner, J. E. (2008). Did magma ascent rate control the explosive-effusive transition at the Inyo volcanic chain, California? *Geology*, *36*(4), 279–282. https://doi.org/10.1130/G24453A.1

Costa, F., Shea, T., & Ubide, T. (2020). Diffusion chronometry and the timescales of magmatic processes. *Nature Reviews Earth & Environment*, *1*(4), 201–214. https://doi.org/10.1038/s43017-020-0038-x

Couch, S., Sparks, R., & Carroll, M. (2003). The kinetics of degassing-induced crystallization at Soufriere Hills Volcano, Montserrat. *Journal of Petrology*, *44*(8), 1477–1502. https://doi.org/10.1093/petrology/44.8.1477

deGraffenried, R., & Shea, T. (2021). Using volatile element concentration profiles in crystal-hosted melt embayments to estimate magma decompression rate: Assumptions and inherited errors. *Geochemistry, Geophysics, Geosystems*, *22*, 1–18. https://doi.org/10.1029/2021GC009672

Ferguson, D. J., Gonnermann, H. M., Ruprecht, P., Plank, T., Hauri, E. H., Houghton, B. F., & Swanson, D. A. (2016). Magma decompression rates during explosive eruptions of Kīlauea volcano, Hawaii, recorded by melt embayments. *Bulletin of Volcanology*, *78*(10), 1–12. https://doi.org/10.1007/s00445-016-1064-x

Gardner, J. E., Hilton, M., & Carroll, M. R. (1999). Experimental constraints on degassing of magma: Isothermal bubble growth during continuous decompression from high pressure. *Earth and Planetary Science Letters*, *168*(1–2), 201–218. https://doi.org/10.1016/S0012-821X(99)00051-5

Geschwind, C.-H., & Rutherford, M. J. (1995). Crystallization of microlites during magma ascent: The fluid mechanics of 1980–1986 eruptions at Mount St Helens. *Bulletin of Volcanology*, *57*(5), 356–370. https://doi.org/10.1007/BF00301293

Geshi, N., Yamasaki, T., Miyagi, I., & Conway, C. E. (2021). Magma chamber decompression during explosive caldera-forming eruption of Aira caldera. *Communications Earth & Environment*, *2*(1), 1–10. https://doi.org/10.1038/s43247-021-00272-x

Hajimirza, S., Gonnermann, H. M., & Gardner, J. E. (2021). Reconciling bubble nucleation in explosive eruptions with geospeedometers. *Nature Communications*, *12*(1), 1–8. https://doi.org/10.1038/s41467-020-20541-1

Hamada, M., Laporte, D., Cluzel, N., Koga, K. T., & Kawamoto, T. (2010). Simulating bubble number density of rhyolitic pumices from Plinian eruptions: Constraints from fast decompression experiments. *Bulletin of Volcanology*, *72*(6), 735–746. https://doi.org/10.1007/s00445-010-0353-z

Hammer, J. E., & Rutherford, M. J. (2002). An experimental study of the kinetics of decompression-induced crystallization in silicic melt. *Journal of Geophysical Research*, *107*(B1), 1–24. https://doi.org/10.1029/2001JB000281

Humphreys, M. C., Menand, T., Blundy, J. D., & Klimm, K. (2008). Magma ascent rates in explosive eruptions: Constraints from H_2O diffusion in melt inclusions. *Earth and Planetary Science Letters*, *270*(1), 25–40. https://doi.org/10.1016/j.epsl.2008.02.041

Iacovino, K., Matthews, S., Wieser, P. E., Moore, G., & Bégué, F. (2021). VESIcal part I: An open-source thermodynamic model engine for mixed volatile (H_2O-CO_2) solubility in silicate melts. *Earth and Space Science*, *8*(11), 1–55. https://doi.org/10.1029/2020EA001584

Jacobs, G. K., & Kerrick, D. M. (1980). A simple rapid-quench design for cold-seal pressure vessels. *American Mineralogist*, *65*(9), 1053–1056.

Leschik, M., Heide, G., Frischat, G., Behrens, H., Wiedenbeck, M., Wagner, N., et al. (2004). Determination of H_2O and D_2O contents in rhyolitic glasses. *Physics and Chemistry of Glasses*, *45*(4), 238–251.

Liu, Y., Anderson, A. T., & Wilson, C. J. (2007). Melt pockets in phenocrysts and decompression rates of silicic magmas before fragmentation. *Journal of Geophysical Research*, *112*(B6), B06204. https://doi.org/10.1029/2006JB004500

Liu, Y., Zhang, Y., & Behrens, H. (2005). Solubility of H_2O in rhyolitic melts at low pressures and a new empirical model for mixed H_2O–CO_2 solubility in rhyolitic melts. *Journal of Volcanology and Geothermal Research*, *143*(1–3), 219–235. https://doi.org/10.1016/j.jvolgeores.2004.09.019

Lloyd, A. S., Ruprecht, P., Hauri, E. H., Rose, W., Gonnermann, H. M., & Plank, T. (2014). NanoSIMS results from olivine-hosted melt embayments: Magma ascent rate during explosive basaltic eruptions. *Journal of Volcanology and Geothermal Research*, *283*, 1–18. https://doi.org/10.1016/j.jvolgeores.2014.06.002

Mangan, M., & Sisson, T. (2000). Delayed, disequilibrium degassing in rhyolite magma: Decompression experiments and implications for explosive volcanism. *Earth and Planetary Science Letters*, *183*(3), 441–455. https://doi.org/10.1016/S0012-821X(00)00299-5

Martel, C., Brooker, R., Andújar, J., Pichavant, M., Scaillet, B., & Blundy, J. (2017). Experimental simulations of magma storage and ascent. In *Volcanic unrest* (pp. 101–110). Springer.

Martel, C., & Schmidt, B. C. (2003). Decompression experiments as an insight into ascent rates of silicic magmas. *Contributions to Mineralogy and Petrology*, *144*(4), 397–415. https://doi.org/10.1007/s00410-002-0404-3

Mastin, L. G. (2005). The controlling effect of viscous dissipation on magma flow in silicic conduits. *Journal of Volcanology and Geothermal Research*, *143*(1–3), 17–28. https://doi.org/10.1016/j.jvolgeores.2004.09.008

McCubbin, F. M., Sverjensky, D. A., Steele, A., & Mysen, B. O. (2014). In-situ characterization of oxalic acid breakdown at elevated P and T: Implications for organic COH fluid sources in petrologic experiments. *American Mineralogist*, *99*(11), 2258–2271. https://doi.org/10.2138/am-2014-4947

McIntosh, I., Llewellin, E., Humphreys, M., Nichols, A., Burgisser, A., Schipper, C., & Larsen, J. (2014). Distribution of dissolved water in magmatic glass records growth and resorption of bubbles. *Earth and Planetary Science Letters*, *401*, 1–11. https://doi.org/10.1016/j.epsl.2014.05.037

Melnik, O., & Sparks, R. (1999). Nonlinear dynamics of lava dome extrusion. *Nature*, *402*(6757), 37–41. https://doi.org/10.1038/46950

Mourtada-Bonnefoi, C. C., & Laporte, D. (2004). Kinetics of bubble nucleation in a rhyolitic melt: An experimental study of the effect of ascent rate. *Earth and Planetary Science Letters*, *218*(3–4), 521–537. https://doi.org/10.1016/S0012-821X(03)00684-8

Moussallam, Y., Rose-Koga, E. F., Koga, K. T., Médard, E., Bani, P., Devidal, J.-L., & Tari, D. (2019). Fast ascent rate during the 2017–2018 Plinian eruption of Ambae (Aoba) volcano: A petrological investigation. *Contributions to Mineralogy and Petrology*, *174*(11), 1–24. https://doi.org/10.1007/s00410-019-1625-z

Myers, M. L., Druitt, T. H., Schiavi, F., Gurioli, L., & Flaherty, T. (2021). Evolution of magma decompression and discharge during a Plinian event (Late Bronze-Age eruption, Santorini) from multiple eruption-intensity proxies. *Bulletin of Volcanology*, *83*(3), 1–17. https://doi.org/10.1007/s00445-021-01438-3

Myers, M. L., Wallace, P. J., Wilson, C. J., Watkins, J. M., & Liu, Y. (2018). Ascent rates of rhyolitic magma at the onset of three caldera-forming eruptions. *American Mineralogist*, *103*(6), 952–965. https://doi.org/10.2138/am-2018-6225

Newcombe, M. E., Plank, T., Barth, A., Asimow, P. D., & Hauri, E. (2020). Water-in-olivine magma ascent chronometry: Every crystal is a clock. *Journal of Volcanology and Geothermal Research*, *398*, 1–17. https://doi.org/10.1016/j.jvolgeores.2020.106872

Nichols, A., & Wysoczanski, R. (2007). Using micro-FTIR spectroscopy to measure volatile contents in small and unexposed inclusions hosted in olivine crystals. *Chemical Geology*, *242*(3–4), 371–384. https://doi.org/10.1016/j.chemgeo.2007.04.007

Ruefer, A., Befus, K., Thompson, J., & Andrews, B. (2021). Implications of multiple disequilibrium textures in quartz-hosted embayments. *Frontiers of Earth Science*, *9*, 1–13. https://doi.org/10.3389/feart.2021.742895

Rutherford, M. J., & Devine, J. D. (2003). Magmatic conditions and magma ascent as indicated by hornblende phase equilibria and reactions in the 1995–2002 Soufriere Hills magma. *Journal of Petrology*, *44*(8), 1433–1454. https://doi.org/10.1093/petrology/44.8.1433

Rutherford, M. J., & Hill, P. M. (1993). Magma ascent rates from amphibole breakdown: An experimental study applied to the 1980–1986 Mount St. Helens eruptions. *Journal of Geophysical Research*, *98*(B11), 19667–19685. https://doi.org/10.1029/93JB01613

Saalfeld, M. A., Myers, M., deGraffenried, R., Shea, T., & Waelkens, C. (2022). On the rise: Using reentrants to extract magma ascent rates in the Bandelier Tuff caldera complex, New Mexico, USA. *Bulletin of Volcanology*, *84*, 1–21. https://doi.org/10.1007/s00445-021-01518-4

Shea, T. (2017). Bubble nucleation in magmas: A dominantly heterogeneous process? *Journal of Volcanology and Geothermal Research*, *343*, 155–170. https://doi.org/10.1016/j.jvolgeores.2017.06.025

Skirius, C. M., Peterson, J. W., & Anderson, A. T. (1990). Homogenizing rhyolitic glass inclusions from the Bishop Tuff. *American Mineralogist*, *75*(11), 1381–1398.

Su, Y., & Huber, C. (2017). The effect of nonlinear decompression history on H_2O/CO_2 vesiculation in rhyolitic magmas. *Journal of Geophysical Research: Solid Earth*, *122*(4), 2712–2723. https://doi.org/10.1002/2016JB013812

Toramaru, A. (2006). BND (bubble number density) decompression rate meter for explosive volcanic eruptions. *Journal of Volcanology and Geothermal Research*, *154*(3), 303–316. https://doi.org/10.1016/j.jvolgeores.2006.03.027

Toramaru, A., Noguchi, S., Oyoshihara, S., & Tsune, A. (2008). MND (microlite number density) water exsolution rate meter. *Journal of Volcanology and Geothermal Research*, *175*(1), 156–167. https://doi.org/10.1016/j.jvolgeores.2008.03.035

Watkins, J. M., Manga, M., & DePaolo, D. J. (2012). Bubble geobarometry: A record of pressure changes, degassing, and regassing at Mono Craters, California. *Geology*, *40*(8), 699–702. https://doi.org/10.1130/G33027.1

Wysoczanski, R., & Tani, K. (2006). Spectroscopic FTIR imaging of water species in silicic volcanic glasses and melt inclusions: An example from the Izu-Bonin arc. *Journal of Volcanology and Geothermal Research*, *156*(3–4), 302–314. https://doi.org/10.1016/j.jvolgeores.2006.03.024

Yoshimura, S., & Nakamura, M. (2010). Chemically driven growth and resorption of bubbles in a multivolatile magmatic system. *Chemical Geology*, *276*(1–2), 18–28. https://doi.org/10.1016/j.chemgeo.2010.05.010

Zhang, Y., & Behrens, H. (2000). H_2O diffusion in rhyolitic melts and glasses. *Chemical Geology*, *169*(1), 243–262. https://doi.org/10.1016/S0009-2541(99)00231-4

Zhang, Y., Jenkins, J., & Xu, Z. (1997). Kinetics of the reaction $H_2O+O \rightarrow 2\ 2OH$ in rhyolitic glasses upon cooling: Geospeedometry and comparison with glass transition. *Geochimica et Cosmochimica Acta*, *61*(11), 2167–2173. https://doi.org/10.1016/S0016-7037(97)00054-9

Zhang, Y., & Ni, H. (2010). Diffusion of H, C, and O components in silicate melts. *Reviews in Mineralogy and Geochemistry*, *72*(1), 171–225. https://doi.org/10.2138/rmg.2010.72.5

Zhang, Y., Xu, Z., & Behrens, H. (2000). Hydrous species geospeedometer in rhyolite: Improved calibration and application. *Geochimica et Cosmochimica Acta*, *64*(19), 3347–3355. https://doi.org/10.1016/S0016-7037(00)00424-5

Zhang, Y., Xu, Z., Zhu, M., & Wang, H. (2007). Silicate melt properties and volcanic eruptions. *Reviews of Geophysics*, *45*(4), 1–27. https://doi.org/10.1029/2006RG000216

Zimmer, M. M., Plank, T., Freymueller, J., Hauri, E. H., Larsen, J. F., & Nye, C. J. (2007). Why do magmas stall? Insights from petrologic and geodetic data.

Zuccarello, F., Schiavi, F., & Viccaro, M. (2022). The eruption run-up at Mt. Etna volcano: Constraining magma decompression rates and their relationships with the final eruptive energy. *Earth and Planetary Science Letters*, *597*, 1–13. https://doi.org/10.1016/j.epsl.2022.117821